Research Article | Vol. 31, No. 7 / 27 Mar 2023 / Optics Express 11335
Optics EXPRESS

Geometric pattern evolution of photonic graphene in coherent atomic medium

HENGFEI ZHANG,[1,2] JINPENG YUAN,[1,2,3] LIANTUAN XIAO,[1,2] SUOTANG JIA,[1,2] AND LIRONG WANG[1,2,4]

[1]State Key Laboratory of Quantum Optics and Quantum Optics Devices, Institute of Laser Spectroscopy, Shanxi University, 92 Wucheng Road, Taiyuan 030006, China
[2]Collaborative Innovation Center of Extreme Optics, Shanxi University, 92 Wucheng Road, Taiyuan 030006, China
[3]yjp@sxu.edu.cn
[4]wlr@sxu.edu.cn

Abstract: The photonic graphene in atoms not only has the typical photonic band structures but also exhibits controllable optical properties that are difficult to achieve in the natural graphene. Here, the evolution process of discrete diffraction patterns of a photonic graphene, which is constructed through a three-beam interference, is demonstrated experimentally in a $5S_{1/2} - 5P_{3/2} - 5D_{5/2}$ ^{85}Rb atomic vapor. The input probe beam experiences a periodic refractive index modulation when traveling through the atomic vapor, and the evolution of output patterns with honeycomb, hybrid-hexagonal, and hexagonal geometric profiles is obtained by controlling the experimental parameters of two-photon detuning and the power of the coupling field. Moreover, the Talbot images of such three kinds of periodic structure patterns at different propagating planes are observed experimentally. This work provides an ideal platform to investigate manipulation the propagation of light in artificial photonic lattices with tunable periodically varying refractive index.

1. Introduction

Propagation of light in dielectric media with a periodically varying refractive index can mimic the physical properties in discrete systems [1,2]. Artificial photonic lattice is a kind of periodic dielectric structure, which possesses all essential characteristics of a nature photonic crystal (e.g., Brillouin zones, and bandgap) but with more beneficial advantages such as the arbitrarily fabricated geometric structuers and simulations of peculiar physics that can not be realized in nature [3–5]. When light injects into a few neighboring sites of lattice, it couples to more and more sites, leading to a spatial broadening of its initial intensity profile [6,7]. Such process is so-called discrete diffraction, which can be deliberately engineered by modifying configuration of the lattice [2,8], allowing one to manipulate the light propagation.

The artificial photonic lattices are mainly investigated in solid materials by the femtosecond laser writing technique. The continuous variation of the refractive index can be achieved by moving the sample transversely to the beam due to the high energy densities in the focal region [9,10]. It has advantages of on-demand and convenient operation but inevitable faces the limitation that the refractive index of the resulting lattices lacking of tunability. On the other hand, the optically induced method in atomic medium has recently emerged as promising alternatives to construct photonics lattices, which arises from utilizing a multi-beam interference dressing field to periodically manipulate the optical response of the medium under the condition of electromagnetically induced transparency (EIT) [11–13]. Such multi-beam interference method can also be used to construct lattices with inversion symmetry broken, which proves a novel platform for research of valley Hall effect and topological insulators in atomic vapors [14,15]. Owing to the instantaneous reconfigurability of coherent multilevel atomic systems, the resulting

#483371 https://doi.org/10.1364/OE.483371
Journal © 2023 Received 13 Dec 2022; revised 12 Feb 2023; accepted 27 Feb 2023; published 20 Mar 2023

Optics EXPRESS

photonic structure are highly tunable, which makes such a structure becoming a good carrier for allowing the manipulation of parameters that are not alterable in solid materials [16–18]. Very recently, some complex electromagnetically induced photonic lattices, such as Kagome and Lieb lattices with localized flatband states, had made preliminary explorations in atomic medium based on spatial light modulator [19,20]. The superior tunability of discrete diffraction patterns of electromagnetically induced photonics lattices has been researched widely in one-dimensional (1D) and square lattice for two-dimensional (2D), which promise realizations of all-optical device [21–25], formation of vector dipole solitons [26,27], and simulation of non-Hermitian physics [28–30].

The photonic graphene, also named as honeycomb lattice, is a kind of artificial photonic lattices with a periodic refractive index of honeycomb profile [9]. Analogous to physical single-layer graphene, the honeycomb lattice has a prominent important role in optics for potential applications in optical capture, optical control, optical communication, and optical integrated circuits [31]. The three-beam interference induced photonic graphene in atomic vapor leading to the observation of topological defects [32], edge states [33], and spin-orbit coupling [34]. Remarkably, the periodic refractive index with honeycomb profile is theoretically adjusted by optical parameters, which can modulate the photonic band structure topology [18,35], resulting the discrete diffraction patterns with honeycomb and hexagonal profiles [13]. Very recently, the inversion of the diffraction patterns from honeycomb to hexagonal profiles was preliminarily investigated [36]. However, the two kinds of patterns are not existed separately. They have a dynamic evolution process that involves complicated hybrid states (the pattern includes both honeycomb and hexagonal profiles, i.e., hybrid-hexagonal profile), which have been theoretically predicted [36] but without experimental observation until now to our best knowledge. This dynamic evolution originates from the refractive index transition of the system, which is exhibited by the continue transformation of discrete diffraction pattern geometry on the space. The hybrid-hexagonal states contain more complex structure, provide driving force in the advancement of atomic topological systems. A complete evolution of discrete diffraction patterns can reveal clearly the dynamic modulation of the medium, and makes the manipulation of light propagation more fascinating.

In this work, we demonstrate a complete evolution of a light wave discrete diffraction in photonic graphene in a three-level cascade-type ^{85}Rb atomic configuration. The evolution is achieved by spatially engineering the refractive index of the photonic graphene, which is optically induced in atomic vapor by the interference of three identical laser beams. By launching a probe beam into the vapor cell, the discrete diffraction patterns under the EIT condition are obtained. A complete evolution of the discrete diffraction patterns from honeycomb to hexagonal profiles is observed by varying the two-photon detuning. In this process, the near resonance of two-photon detuning and large power of coupling field ensure the acquisition of patterns with hybrid-hexagonal profile. Finally, these diffraction patterns, as typical periodic structures, whose Talbot effects are also studied experimentally. This work paves a way for precisely manipulating of light dynamics in photonics lattice with tunable spatially modulated refractive index.

2. Experimental setup

Figure 1(a) shows the experimental setup in a three-level cascade-type ^{85}Rb atomic configuration, which consisting of $|1\rangle = |5S_{1/2}\rangle(F = 2)$, $|2\rangle = |5P_{3/2}\rangle(F = 3)$, and $|3\rangle = |5D_{5/2}\rangle(F = 4)$ [Fig. 1(b)]. The coupling field $\boldsymbol{E_c}$ (with wavelength $\lambda_c = 776$ nm, frequency ω_c), from a tapered-amplified diode laser (TA pro, Toptica), is first split into two beams by the combination of a half-wave plate (HWP1) and a polarization beam splitter (PBS1). One beam is used for EIT reference. As shown in the inset of Fig. 1(a), the EIT spectrum is obtained by locking the probe beam frequency on the transition of $|1\rangle \rightarrow |2\rangle$ and scanning the frequency of coupling beam around the transition of $|2\rangle \rightarrow |3\rangle$ to ensure the frequency of coupling field. The other beam,

Optics EXPRESS

frequency shifted by an acousto-optical modulator in a double-pass configuration, is split by beam splitters (BS1-BS6) into three beams $\boldsymbol{E_{c1}}$, $\boldsymbol{E_{c2}}$, and $\boldsymbol{E_{c3}}$ with detuning of $\Delta_c = \omega_c - \omega_{23}$, where ω_{ij} $(i,j = 1,2,3)$ are the resonant frequencies between the levels $|i\rangle$ and $|j\rangle$. As shown in Fig. 1(c), these three beams propagate along z-direction with a small angle between each other, forming an interference coupling field in atomic vapor to induce the photonic graphene. Figure 1(d) is the simulated intensity distribution of the three-beam interference coupling field, which shows a hexagonal profile in the $x - y$ plane but with dark-triangular sites around bright sites to form a honeycomb profile [13,18]. Here, the Rb vapor cell is heated by an oven to provide an atomic density of about 3.56×10^{12} cm^{-3} at 92 °C, and the elastic collisions are predominant under this condition. The corresponding experimental observation by a charge-coupled device (CCD) shown in Fig. 1(e) agree well with the theoretical simulation, and a definite period of $d \approx 202$ μm is given by experimental measurement.

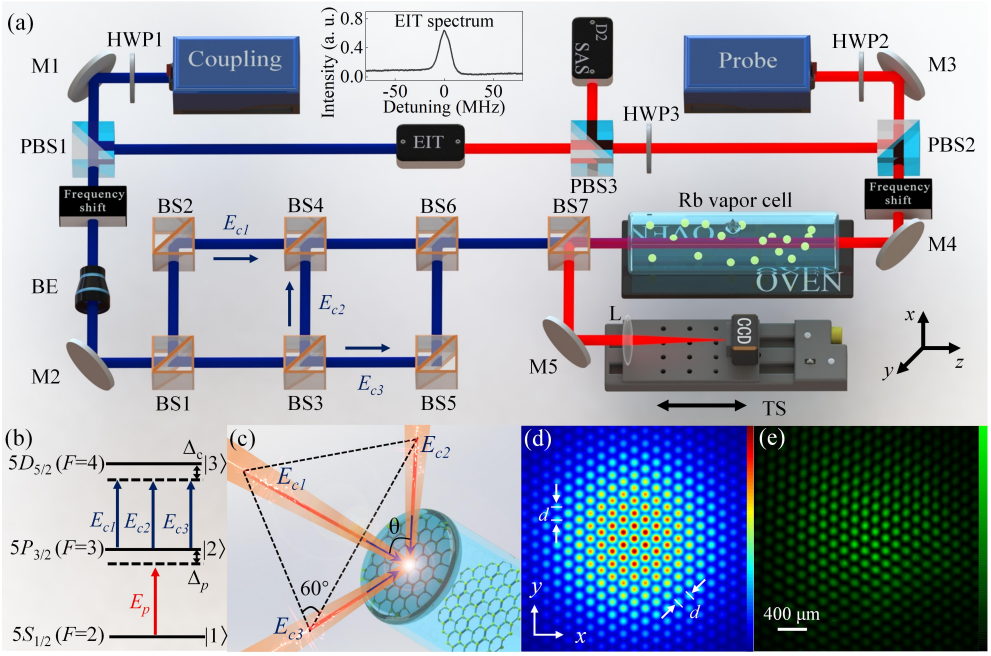

Fig. 1. (a) Experiment setup, HWP: half-wave plate; M: high reflection mirror; PBS: polarization beam splitter; EIT: electromagnetically induced transparency; BE: beam expander; BS: 50/50 beam splitter; SAS: saturation absorption spectroscopy; L: lens; CCD: charge-coupled device; TS: translation stage. (b) Relevant energy levels of the cascade-type three-level configuration in ^{85}Rb atoms. (c) Schematic plot of the photonic graphene by three-beam interference method. (d), (e) Theoretical simulated and corresponding experimental observed intensity distribution of interference coupling field.

The probe field $\boldsymbol{E_p}$ (with wavelength $\lambda_p = 780$ nm, frequency ω_p) from an external cavity diode laser (DL pro, Toptica) is also spilt into two beams by the combination of a half-wave plate (HWP2) and a polarization beam splitter (PBS2). One beam is used for saturation absorption spectroscopy (SAS) and EIT reference. The frequency of probe beam is locked by the SAS accurately. While the other beam with detuning of $\Delta_p = \omega_p - \omega_{12}$ counter-propagates with the coupling field inside the atomic vapor. It experiences a spatially modulated refractive index under the EIT condition, and the discrete diffraction pattern of probe beam is imaged onto a CCD via an imaging lens. Here, the focal length of the imaging lens is 100 mm, and the distance between the lens and the CCD is twice of focal length. A translation stage (TS) is used to move simultaneously

Optics EXPRESS

the imaging lens and CCD along the z-direction to obtain the propagating behaviors of the output patterns at different observing planes in free space.

3. Results and discussions

The optical response of the probe field in this three-level cascade-type atomic configuration can be described through the spatially modulated susceptibility as [16]

$$\chi = \frac{iN|\mu_{12}|^2}{\hbar\varepsilon_0}[\gamma_{21} - i\Delta_p + \frac{|\Omega_{eff}|^2}{\gamma_{31} - i(\Delta_p + \Delta_c)}]^{-1}, \tag{1}$$

where N is the atomic density, ε_0 is the permittivity of free space, μ_{12} is the transition dipole momentum between levels $|1\rangle$ and $|2\rangle$, $\gamma_{ij} = \frac{1}{2}(\Gamma_i + \Gamma_j)$ with Γ_i are the spontaneous decay rates of the population from the excited states to ground state during the transition, which are $\Gamma_1 = 0$ (since level $|1\rangle$ is ground state), $\Gamma_2 = 2\pi \times 6.06$ MHz, and $\Gamma_3 = 2\pi \times 0.45$ MHz, respectively, and $\Omega_{eff} = \sum_{m=1}^{3} \Omega_c exp[ik_0 \overrightarrow{b_m} \cdot \overrightarrow{r}]$ is the effective Rabi frequency of the three-beam interference coupling field, in which Ω_c represents the Rabi frequency of each coupling beams, $\overrightarrow{b_1} = (1, 0)$, $\overrightarrow{b_2} = (-\frac{1}{2}, \frac{\sqrt{3}}{2})$, and $\overrightarrow{b_3} = (-\frac{1}{2}, -\frac{\sqrt{3}}{2})$.

The key point of the experiment is to periodically modulate the refractive index experienced by the probe beam. Figure 2 shows the simulated spatial refractive indices, mainly determined by the real part of susceptibility [$Re(\chi)$] with a negligibly small imaginary part [$Im(\chi)$] [32], for different two-photon detunings of $\Delta = \Delta_p + \Delta_c$. In Figs. 2(a) and 2(b), with Δ<0, the refractive index exhibit honeycomb profiles. Its values at the honeycomb sites are big and in the hexagonal ones are small. When Δ>0, as shown in Figs. 2(c) and 2(d), the sites with the maximum and the minimum values of refractive index are inverted with those for Δ<0, but still exhibits honeycomb-like profiles [18,35,37]. In other words, the refractive index can be modulated by the two-photon detuning, which will further determine the observed geometric profile of discrete diffraction patterns.

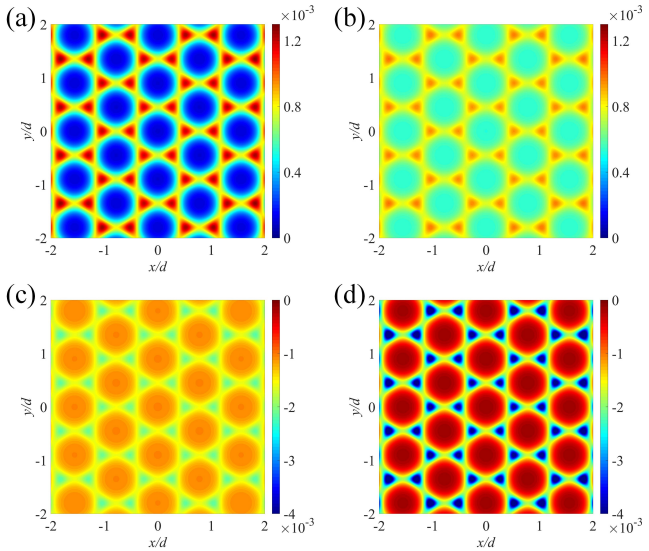

Fig. 2. Simulated spatial refractive indices of the probe beam experienced in photonic graphene with different two-photon detunings of (a) $\Delta = -2\Gamma_2$, (b) $\Delta = -\Gamma_2$, (c) $\Delta = 0.5\Gamma_2$, and (d) $\Delta = \Gamma_2$. The other parameters are $\Omega_c = 3\Gamma_2$, $\Gamma_1 = 0$, and $\Gamma_3 = 0.07\Gamma_2$.

Optics EXPRESS

According to the Fresnel-Kirchhoff diffraction and under the paraxial approximation, the diffraction intensity distribution of the probe beam at the observation plane with a distance of z from the output surface can be expressed as [12]

$$I(X,Y,z) \propto \int_{-\infty}^{+\infty}\int_{-\infty}^{+\infty} T(x,y)exp[ik_p(z+\frac{x^2+y^2}{2z}-\frac{xX+yY}{2z}+\frac{X^2+Y^2}{2z})]dxdy, \quad (2)$$

where (x, y) and (X, Y) are the coordinates in the object and observation planes, respectively, $T(x,y) = exp[-k_p Im(\chi)L + ik_p Re(\chi)L]$ is the transmission function of the probe field, $k_p = 2\pi/\lambda_p$ is the wavenumber of the probe beam, and L is the thickness of atomic medium. For completing the integral in Eq. (2), the $T(x, y)$ can be expanded into a 2D Fourier series as [13]

$$T(x,y) = \sum_{m,n=-\infty}^{+\infty} C_{mn}exp[i2\pi(\frac{m}{d}x+\frac{n}{\sqrt{3}d}y)], \quad (3)$$

where C_{mn} is a 2D Fourier coefficient. By substituting Eq. (2) into Eq. (3), we can obtain the diffraction intensity distribution along z as

$$I(X,Y,z) \propto C_0 \sum_{m,n=-\infty}^{+\infty} C_{mn}exp[-i\pi\lambda_p z(\frac{m^2}{d^2}+\frac{n^2}{3d^2})] \times exp[i2\pi(\frac{m}{d}X+\frac{n}{\sqrt{3}d}Y)], \quad (4)$$

where the irrelevant terms have been absorbed into C_0. As the refractive index information are contained in the 2D Fourier coefficient, the discrete diffraction patterns of probe beam can be modulated through the parameters of photonic graphene.

Figures 3(a-e) are the numerically simulated diffraction patterns according to Eq. (4) under different two-photon detunings at the output plane of the vapor cell ($z = 0$). The competition between the intensities of honeycomb and hexagonal sites in modulated refractive index leads to the geometric profile evolution of diffraction patterns. As shown in Fig. 3(a), the pattern with a clear honeycomb profile is obtained for $\Delta = -2\Gamma_2$, since the refractive index at the honeycomb sites is the biggest and in the hexagonal sites is nearly zero [see Fig. 2(a)]. The hybrid-hexagonal profile, which presents as the hexagonal distribution appears in the honeycomb profile, is obtained as shown in Fig. 3(b) of $\Delta = -\Gamma_2$. In this case the refractive index at the honeycomb sites becomes small while in the hexagonal sites increases [see Fig. 2(b)]. The hexagonal intensity in hybrid-hexagonal profile increases with the two-photon detuning more closer to the resonance, as shown in Fig. 3(c) of $\Delta = -0.5\Gamma_2$. Further, the refractive index at the hexagonal sites is stronger than that in honeycomb sites when $\Delta>0$ [see Fig. 2(c)]. Thus, the hexagonal intensity in hybrid-hexagonal profile is stronger than honeycomb intensity, as shown in Fig. 3(d) of $\Delta = 0.5\Gamma_2$. Finally, the pattern with a clear hexagonal profile is obtained as shown in Fig. 3(e) of $\Delta = \Gamma_2$, since the refractive index at the hexagonal sites is biggest while in the honeycomb sites is nearly zero with the two-photon detuning far from the resonance [see Fig. 2(d)]. Figures 3(f-j) are the experimental observations by varying the two-photon detuning. A complete evolution of diffraction patterns from honeycomb to hexagonal profiles in photonic graphene is obtained experimentally, which agree well with numerical simulations graphically.

The patterns with hybrid-hexagonal geometric profile in the above evolution process, to the best of our knowledge, are first discovered in our proposed system. In fact, in addition to the near-resonant two-photon detuning, the power of the coupling field, determined by Ω_{eff} in Eq. (1) affects the intensity distribution of the refractive index experienced by the probe beam, also plays a key role in the acquisition of such hybrid-hexagonal profiles. Figure 4 shows the observed diffraction patterns with the different powers of the coupling field P_c when $\Delta = -5$ MHz. A fuzzy honeycomb profile is observed when $P_c = 12$ mW [see Fig. 4(a)]. Such a weak coupling field results the refractive index with a small value, which is not strong enough to guide the whole

Optics EXPRESS

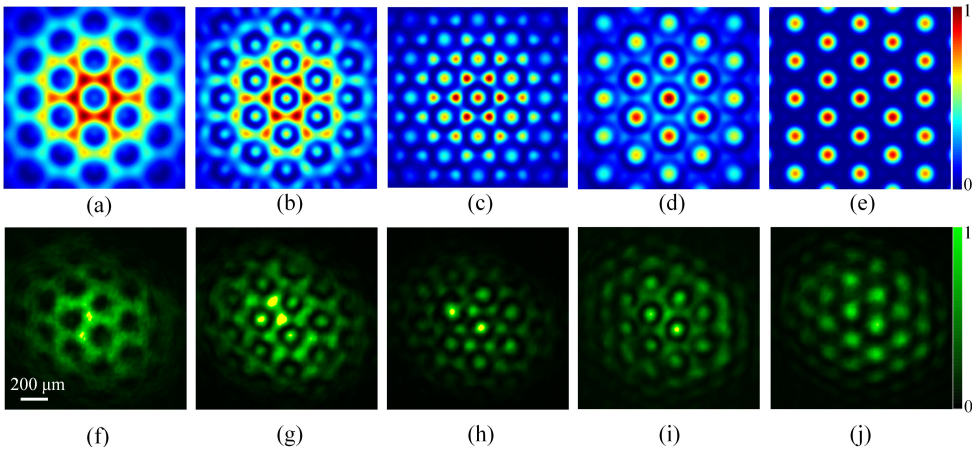

Fig. 3. (a-e) Numerically simulated diffraction patterns of probe beam at $z = 0$ [Eq. (4)] with different two-photon frequency detuning of (a) $\Delta = -2\Gamma_2$, (b) $\Delta = -\Gamma_2$, (c) $\Delta = -0.5\Gamma_2$, (d) $\Delta = 0.5\Gamma_2$, and (e) $\Delta = \Gamma_2$. (f-j) Experimentally observed diffraction patterns with (f) $\Delta = -30$ MHz, (g) $\Delta = -15$ MHz, (h) $\Delta = -5$ MHz, (i) $\Delta = 5$ MHz, and (j) $\Delta = 15$ MHz. Here, the powers of the coupling and probe fields are $P_c = 75$ mW and $P_p = 7$ mW in experiments, respectively.

probe beam into individual channel to diffract. A clear honeycomb profile is observed when P_c is increased to 21 mW [see Fig. 4(b)]. In this case, the refractive index at the honeycomb sites becomes strong while in the hexagonal sites is nearly zero. The hybrid-hexagonal profiles gradually appear shown in Figs. 4(c)–4(e), for the increasing P_c that makes the refractive index in hexagonal sites begins to increase. The larger P_c, the stronger the intensity of the hexagonal sites in refractive index, and the hexagonal intensity in hybrid-hexagonal profile reaches the maximum under a large power of $P_c = 75$ mW [see Fig. 4(f)]. Moreover, the diffraction patterns will be destroyed with further increasing P_c, which is mainly because stronger coupling field will render a wide opening individual channel that concentrates the light on the forward direction and limits the chances of light to stray into the higher order [16]. Note that, the diffraction patterns can't evolve from honeycomb to hexagonal profiles with only varying P_c, since coupling field only changes the intensity distribution of refractive index while not invert it like two-photon detuning.

The photonic graphene in atomic vapor, as a typical periodic structure, whose diffraction patterns can propagate periodically along the z-direction and reproduces the initial patterns at certain planes. Such process is so-called Talbot effect [38,39], in which the self-imaging planes are located at integer multiples of the Talbot length, calculated in our system as $Z_T = m \times 3d^2/(2\lambda_p) \approx m \times 78.5$ mm, where d is the spatial period of photonic lattice and m is a positive integer [40]. The Talbot image of three typical periodic structure patterns of honeycomb, hybrid-hexagonal, and hexagonal profiles [Figs. 3(f), (h), and (j)] are further investigated by moving the imaging lens and CCD simultaneously along z-direction. As shown in Fig. 5(a), the pattern with honeycomb profile at $z = 80$ mm reproduces the pattern at $z = 0$, indicating the measured Talbot length is about 80 mm basically agreeing with the theoretically calculation. A slight error from the measured position and the calculated one is coming from the measurement deviation of length. The relatively weak intensity of reproduced pattern is caused by the divergence of the probe beam in transmission. The hybrid-hexagonal and hexagonal profiles are observed respectively at $z = 20$ mm and 40 mm [41,42], and more complicated Talbot sub-images are obtained at $z = 50$ mm and 65 mm. Figures 5(b) and 5(c) are the observed Talbot images of initial pattern with hybrid-hexagonal and

Optics EXPRESS

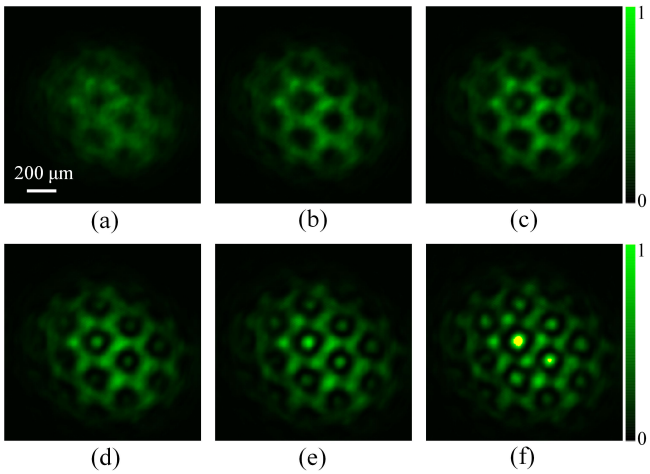

Fig. 4. Experimentally observed diffraction patterns of probe beam with different coupling field powers of (a) 12 mW, (b) 21 mW, (c) 30 mW, (d) 45 mW, (e) 60 mW, and (f) 75 mW.

hexagonal profiles respectively. They also show the reproduction at z = 80 mm, and have the similar dynamic evolution of that shown in Fig. 5(a) [43].

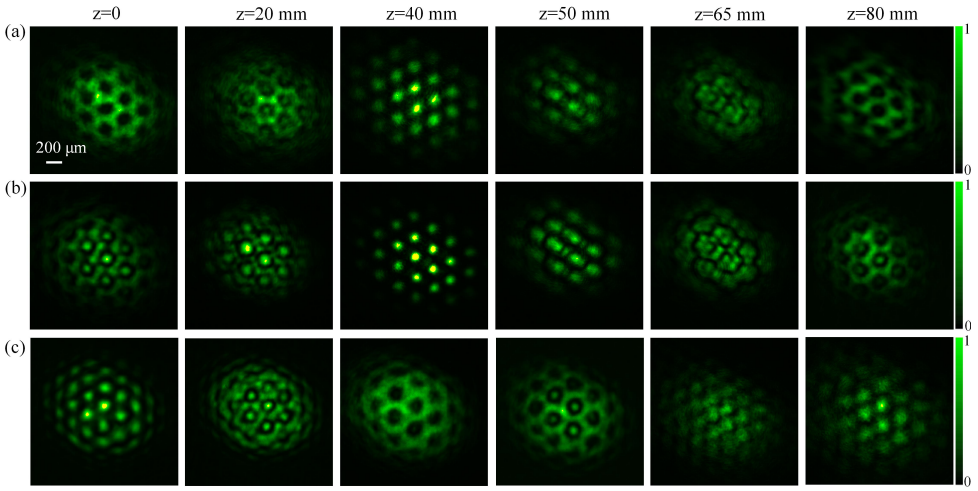

Fig. 5. Talbot images of diffraction patterns with (a) honeycomb [Fig. 3(f)], (b) hybrid-hexagonal [Fig. 3(h)], and (c) hexagonal profiles [Fig. 3(j)] at different propagation distances z.

4. Conclusions

In conclusion, the evolution of discrete diffraction patterns of light wave in photonic graphene is demonstrated in a three-level cascade-type ^{85}Rb atomic configuration. Three coupling beams propagating along the z direction are responsible for optically inducing the photonic graphene. The input probe beam traveling through photonic graphene with a tunable spatially modulated refractive index, and the discrete diffraction patterns are observed at the output plane of the cell. A complete evolution of patterns from honeycomb to hexagonal profiles is observed owed to the variation of the spatial refractive index by changing two-photon detuning. And the large coupling field power over 45 mW in near two-photon resonance case ensures the acquisition

Optics EXPRESS

of hybrid-hexagonal profiles. Moreover, the diffraction patterns with three typical periodic structures are all reproduced, and complicated Talbot sub-images are also observed. This work can be used to investigate intriguing nonlinear and quantum beam dynamical features that are predicted for constructed periodic optical systems.

Funding. National Natural Science Foundation of China (62075121); Open Fund of MOE Key Laboratory of Weak-Light Nonlinear Photonics (OS 22-2); Shanxi "1331 Project".

Disclosures. The authors declare no conflicts of interest.

Data availability. Data underlying the results presented in this paper are not publicly available at this time but may be obtained from the authors upon reasonable request.

References

1. D. N. Christodoulides, F. Lederer, and Y. Silberberg, "Discretizing light behaviour in linear and nonlinear waveguide lattices," Nature **424**(6950), 817–823 (2003).
2. I. L. Garanovich, S. Longhi, A. A. Sukhorukov, and Y. S. Kivshar, "Light propagation and localization in modulated photonic lattices and waveguides," Phys. Rep. **518**(1-2), 1–79 (2012).
3. W. B. Gao, A. Imamoglu, H. Bernien, and R. Hanson, "Coherent manipulation, measurement and entanglement of individual solid-state spins using optical fields," Nat. Photonics **9**(6), 363–373 (2015).
4. D. D. Awschalom, R. Hanson, J. Wrachtrup, and B. B. Zhou, "Quantum technologies with optically interfaced solid-state spins," Nat. Photonics **12**(9), 516–527 (2018).
5. J. Everett, G. T. Campbell, Y.-W. Cho, P. Vernaz-Gris, D. B. Higginbottom, O. Pinel, N. P. Robins, P. K. Lam, and B. C. Buchler, "Dynamical observations of self-stabilizing stationary light," Nat. Phys. **13**(1), 68–73 (2017).
6. T. Pertsch, T. Zentgraf, U. Peschel, A. Bräuer, and F. Lederer, "Anomalous refraction and diffraction in discrete optical systems," Phys. Rev. Lett. **88**(9), 093901 (2002).
7. A. Zannotti, J. M. Vasiljević, D. V. Timotijević, D. M. J. Savić, and C. Denz, "Morphing discrete diffraction in nonlinear Mathieu lattices," Opt. Lett. **44**(7), 1592–1595 (2019).
8. H. S. Eisenberg, Y. Silberberg, R. Morandotti, A. R. Boyd, and J. S. Aitchison, "Discrete spatial optical solitons in waveguide arrays," Phys. Rev. Lett. **81**(16), 3383–3386 (1998).
9. Y. Plotnik, M. C. Rechtsman, D. Song, M. Heinrich, J. M. Zeuner, S. Nolte, Y. Lumer, N. Malkova, J. Xu, A. Szameit, Z. Chen, and M. Segev, "Observation of unconventional edge states in 'photonic graphene'," Nat. Mater. **13**(1), 57–62 (2014).
10. D. Song, V. Paltoglou, S. Liu, Y. Zhu, D. Gallardo, L. Tang, J. Xu, M. Ablowitz, N. K. Efremidis, and Z. Chen, "Unveiling pseudospin and angular momentum in photonic graphene," Nat. Commun. **6**(1), 6272 (2015).
11. H. Y. Ling, Y.-Q. Li, and M. Xiao, "Electromagnetically induced grating: Homogeneously broadened medium," Phys. Rev. A **57**(2), 1338–1344 (1998).
12. F. Wen, H. Ye, X. Zhang, W. Wang, S. Li, H. Wang, Y. Zhang, and C.-W. Qiu, "Optically induced atomic lattice with tunable near-field and far-field diffraction patterns," Photonics Res. **5**(6), 676–683 (2017).
13. F. Wen, X. Zhang, H. Ye, W. Wang, H. Wang, Y. Zhang, Z. Dai, and C.-W. Qiu, "Efficient and tunable photoinduced honeycomb lattice in an atomic ensemble," Laser Photonics Rev. **12**(9), 1800050 (2018).
14. H. Zhong, Y. Zhang, M. R. Belić, and Y. Zhang, "Generating Lieb and super-honeycomb lattices by employing the fractional Talbot effect," J. Opt. Soc. Am. B **36**(4), 862–866 (2019).
15. H. Zhong, Y. V. Kartashov, Y. Zhang, D. Song, Y. Zhang, F. Li, and Z. Chen, "Rabi-like oscillation of photonic topological valley Hall edge states," Opt. Lett. **44**(13), 3342–3345 (2019).
16. J. Yuan, C. Wu, L. Wang, G. Chen, and S. Jia, "Observation of diffraction pattern in two-dimensional optically induced atomic lattice," Opt. Lett. **44**(17), 4123–4126 (2019).
17. J. Yuan, S. Dong, C. Wu, L. Wang, L. Xiao, and S. Jia, "Optically tunable grating in a V+Ξ configuration involving a Rydberg state," Opt. Express **28**(16), 23820–23828 (2020).
18. Y. Zhang, X. Liu, M. R. Belic, Z. Wu, and Y. Zhang, "Modulation of the photonic band structure topology of a honeycomb lattice in an atomic vapor," Ann. Phys. **363**, 114–121 (2015).
19. Q. Yu, Z. Liu, D. Guo, S. Liang, Y. Zhang, and Z. Zhang, "Optically-induced symmetry switching in a reconfigurable Kagome photonic lattice: From flatband to type-III Dirac cones," Nanomaterials **12**(18), 3222 (2022).
20. S. Liang, Z. Liu, S. Ning, Y. Zhang, and Z. Zhang, "Experimental realization of a reconfigurable Lieb photonic lattice in a coherent atomic medium," Opt. Lett. **48**(3), 803–806 (2023).
21. J. Sheng, U. Khadka, and M. Xiao, "Realization of all-optical multistate switching in an atomic coherent medium," Phys. Rev. Lett. **109**(22), 223906 (2012).
22. J. Yuan, S. Dong, H. Zhang, C. Wu, L. Wang, L. Xiao, and S. Jia, "Efficient all-optical modulator based on a periodic dielectric atomic lattice," Opt. Express **29**(2), 2712–2719 (2021).
23. H. Zhang, J. Yuan, S. Dong, C. Wu, L. Wang, L. Xiao, and S. Jia, "All-optical tunable high-order Gaussian beam splitter based on a periodic dielectric atomic structure," Opt. Express **29**(16), 25439–25448 (2021).
24. J. Yuan, H. Zhang, C. Wu, L. Wang, L. Xiao, and S. Jia, "Tunable optical vortex array in a two-dimensional electromagnetically induced atomic lattice," Opt. Lett. **46**(17), 4184–4187 (2021).

Optics EXPRESS

25. J. Yuan, H. Zhang, C. Wu, G. Chen, L. Wang, L. Xiao, and S. Jia, "Creation and control of vortex-beam arrays in atomic vapor," Laser Photonics Rev. **2023** 2200667 (2023).
26. D.-W. Wang, H.-T. Zhou, M.-J. Guo, J.-X. Zhang, J. Evers, and S.-Y. Zhu, "Optical diode made from a moving photonic crystal," Phys. Rev. Lett. **110**(9), 093901 (2013).
27. Y. Zhang, Z. Wang, Z. Nie, C. Li, H. Chen, K. Lu, and M. Xiao, "Four-wave mixing dipole soliton in laser-induced atomic gratings," Phys. Rev. Lett. **106**(9), 093904 (2011).
28. Y.-M. Liu, F. Gao, J.-H. Wu, M. Artoni, and G. C. La Rocca, "Lopsided diffractions of distinct symmetries in two-dimensional non-Hermitian optical gratings," Phys. Rev. A **100**(4), 043801 (2019).
29. Z. Zhang, D. Ma, J. Sheng, Y. Zhang, Y. Zhang, and M. Xiao, "Non-Hermitian optics in atomic systems," J. Phys. B: At., Mol. Opt. Phys. **51**(7), 072001 (2018).
30. Z. Zhang, Y. Zhang, J. Sheng, L. Yang, M.-A. Miri, D. N. Christodoulides, B. He, Y. Zhang, and M. Xiao, "Observation of parity-time symmetry in optically induced atomic lattices," Phys. Rev. Lett. **117**(12), 123601 (2016).
31. A. Turpin, Y. V. Loiko, T. K. Kalkandjiev, and J. Mompart, "Conical refraction: fundamentals and applications," Laser Photonics Rev. **10**(5), 750–771 (2016).
32. Z. Zhang, F. Li, G. Malpuech, Y. Zhang, O. Bleu, S. Koniakhin, C. Li, Y. Zhang, M. Xiao, and D. D. Solnyshkov, "Particlelike behavior of topological defects in linear wave packets in photonic graphene," Phys. Rev. Lett. **122**(23), 233905 (2019).
33. Z. Zhang, R. Wang, Y. Zhang, Y. V. Kartashov, F. Li, H. Zhong, H. Guan, K. Gao, F. Li, Y. Zhang, and M. Xiao, "Observation of edge solitons in photonic graphene," Nat. Commun. **11**(1), 1902 (2020).
34. Z. Zhang, S. Liang, F. Li, S. Ning, Y. Li, G. Malpuech, Y. Zhang, M. Xiao, and D. Solnyshkov, "Spin-orbit coupling in photonic graphene," Optica **7**(5), 455–462 (2020).
35. Y. Zhang, Z. Wu, M. R. Belic, H. Zheng, Z. Wang, M. Xiao, and Y. Zhang, "Photonic Floquet topological insulators in atomic ensembles," Laser Photonics Rev. **9**(3), 331–338 (2015).
36. Z. Zhang, Y. Feng, S. Ning, G. Malpuech, D. D. Solnyshkov, Z. Xu, Y. Zhang, and M. Xiao, "Imaging lattice switching with Talbot effect in reconfigurable non-Hermitian photonic graphene," Photonics Res. **10**(4), 958–964 (2022).
37. S. Ning, J. Lu, S. Liang, Y. Feng, C. Li, Z. Zhang, and Y. Zhang, "Talbot effect of an electromagnetically induced square photonic lattice assisted by a spatial light modulator," Opt. Lett. **46**(19), 5035–5038 (2021).
38. H. F. Talbot, "Facts relating to optical science," Philos. Mag. J. Sci. **9**(56), 401–407 (1836).
39. J. Wen, S. Du, H. Chen, and M. Xiao, "Electromagnetically induced Talbot effect," Appl. Phys. Lett. **98**(8), 081108 (2011).
40. C.-S. Guo, X. Yin, L.-W. Zhu, and Z.-P. Hong, "Analytical expression for phase distribution of a hexagonal array at fractional Talbot planes," Opt. Lett. **32**(15), 2079–2081 (2007).
41. J. Yuan, C. Wu, Y. Li, L. Wang, Y. Zhang, L. Xiao, and S. Jia, "Integer and fractional electromagnetically induced Talbot effects in a ladder-type coherent atomic system," Opt. Express **27**(1), 92–101 (2019).
42. Y. Zhang, J. Wen, S. N. Zhu, and M. Xiao, "Nonlinear Talbot effect," Phys. Rev. Lett. **104**(18), 183901 (2010).
43. J. Belín and T. Tyc, "Talbot effect for gratings with diagonal symmetry," J. Opt. **20**(2), 025604 (2018).